Performance Evaluation of a Low-Speed Single-Side HTS Linear Induction Motor Used for Subway System

Dong Li, Weili Li, Jin Fang, Xiaochen Zhang, and Junci Cao

School of Electrical Engineering, Beijing Jiaotong University, Beijing 100044, China

Due to the critical characteristics and the magnetic flux pinning phenomenon of the high-temperature superconducting (HTS) material, the electromagnetic calculation for the HTS motor is more complicated than for conventional motors. In this paper, the equivalent electrical conductivity and the equivalent magnetic permeability are proposed to represent the critical characteristics and the magnetic flux pinning phenomenon, respectively. Considering the low-speed single-sided HTS linear induction motor as an example, the 2-D mathematical model is established and its boundary conditions are given. The model is solved using the time-step finite-element method. The flux density distributions and the performance parameters, such as thrust, vertical force, eddy-current loss, efficiency, power factor, and so on, are obtained. In addition, the magnetic flux density around the HTS windings is also calculated to evaluate the influence of the leakage magnetic flux on the critical current. Finally, the experiment is carried out to validate the accuracy of the established model.

Index Terms—Equivalent electrical conductivity, equivalent magnetic permeability, finite element method, HTS linear induction motor, performance parameters.

I. INTRODUCTION

THE LINEAR induction motor (LIM) is derived from the rotating induction motor (RIM). Instead of producing rotation torque, it produces a linear force along the moving direction. Thus, the linear induction motor could drive the wheeled vehicles with independent wheel-rail adhesion. Therefore, the LIM finds wide applications in the transportation system [1]–[6]. In high-speed applications, it is difficult to supply electrical power. Thus, the LIM with short secondary (rotor in RIM) and long primary (stator in RIM) are developed as vehicle drives [6]–[8]. The construction cost of the transportation system is very high and the requirements of the control technique become complicated and strict due to the structure of the long primary LIM. In low-speed applications, such as subway system, the power supply by pantograph catenary system and the third rail has been used for many years. This power supply could also satisfy the requirements of the LIM with short primary. Thus, the construction cost of the subway system propelled by the short-primary LIM can be dramatically cut down. Moreover, the secondary could be developed by reconstructing the inherent routes without need to construct new ones, which will further reduce the construction cost of the transportation system. Therefore, the LIM with short primary has found wider applications in the transportation system than the LIM with long primary, e.g., the linear metro in Japan, then Vancouver light train in Canada, and the Guangzhou subway line 4 and the Airport Beijing City [9], [10]. Compared with the subway driven by conventional rotating motors, the subway driven by the LIM has the following advantages: 1) the construction cost could be greatly decreased by making the height of the tunnel

lower and 2) the metro small turning circle, strong climbing ability, and low noise, so the route line would be more flexible [11]. To ensure the subway to operate safely and with stable performance, the LIM is usually designed with an air-gap ranging from 10 to 100 mm, which is larger than the RIM. During the energy conversion process, the magnetic energy is carried away and lost at the ends of the primary by the relative movement of the primary and secondary. This phenomenon is called "end effects." All these above finally make the LIM show two major drawbacks, low efficiency and power factors. These two drawbacks are the cause of high energy consumptions [12]. The eddy-current loss in the secondary plate as well as the thrust is tightly related to the frequency. The LIM will have high efficiency and a large thrust at low frequencies [5]. Moreover, if the subway station is not far away from the next one, the low speed could satisfy the requirements. For these reasons, the LIM considered for the subway system is designed for low frequency operation. Due to the large exciting current in the primary windings, the efficiency of the motor at low frequency is still lower than that of the rotating motors. Taking advantage of the zero resistance of the high temperature materials, the efficiency could be greatly improved by reducing the loss of the primary windings [13]. With the properties and the manufacturing technology of the HTS materials improved, the construction cost of the HTS electrical devices has been significantly cut down. Therefore, number of types of HTS motors developed using the HTS tapes or HTS magnets have been fabricated [14]–[17]. The HTS linear synchronous motor, with the permanent magnets replaced using the HTS magnets or HTS tapes for dc use, has been successfully constructed and the motor could be operated with a better performance [18], [19]. However, there were only a few attempts to develop the HTS LIM using the HTS tapes for ac use [20]. Recently, the properties of the HTS tapes for ac use were greatly improved. The HTS LIM with HTS tapes has become feasible, especially for the low-frequency applications for the subway system [21]. Due to the low ac loss and
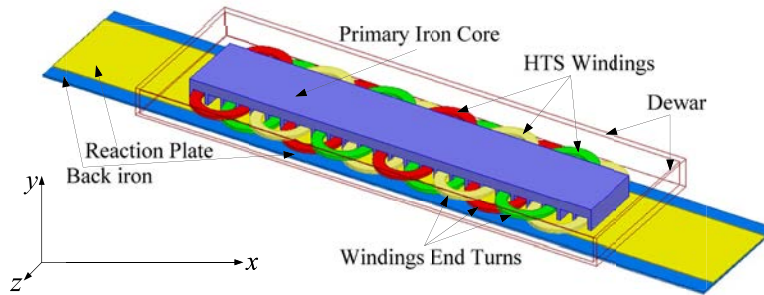
Fig. 1.   Basic physical structure of the HTS LIM with a slotted iron core.
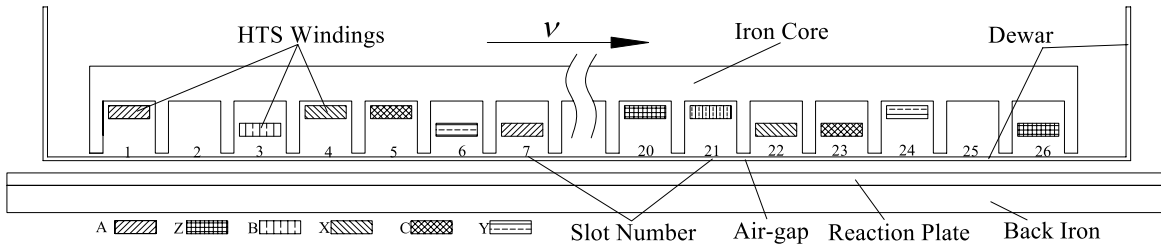

Fig. 2.   Sectional overview of the HTS LIM.

the high current density, the HTS LIM has the advantages such as low volume, light weight, high efficiency and high power density, and so on [16], [22]. The material properties as the electrical conductivity and the magnetic permeability are more complicated than the conventional materials. To evaluate the performance of the HTS LIM, the traditional analysis methods should be modified by considering the material properties of the high temperature superconductors.

In this paper, a low-speed single-sided HTS LIM, with excitation windings from Bi-2223/Ag HTS tapes and distributed as a double-layer concentrating structure, is proposed. The mathematical model considering the current characteristics and the magnetic flux pinning phenomenon of the superconductor is established to evaluate the performance of the HTS LIM. The model is solved using the 2-D time-stepping finite-element method (FEM). In addition, the experiment is also designed to evaluate the accuracy of the FEM simulation results.

II. MATHEMATICAL MODEL FOR THE HTS LIM

A. Physical Structure of the HTS LIM

The developed HTS LIM is a short primary (stator in rotating motors) and a long secondary (rotor in rotating motors), as shown in Fig. 1. Fig. 2 shows the sectional overview of the machine. The primary windings are constructed using the bi-2223 HTS tapes and cured using the dip-coating method. The critical current decreases as the leakage magnetic flux density increasing. The iron core is designed to reduce the leakage magnetic flux around the HTS windings. The iron core is made of the laminated silicon steel sheet to reduce the eddy-current loss. The HTS windings are designed with the same pitch due to the processing requirements. While the 12 HTS coils are assembled in the slots, the slots No. 2 and No. 25 are vacant. The distributed structure has the mechanical as well as electrical symmetry. The HTS windings and the iron core comprise the primary of the motor. The entire primary is immersed in the Dewar vessel which is filled with
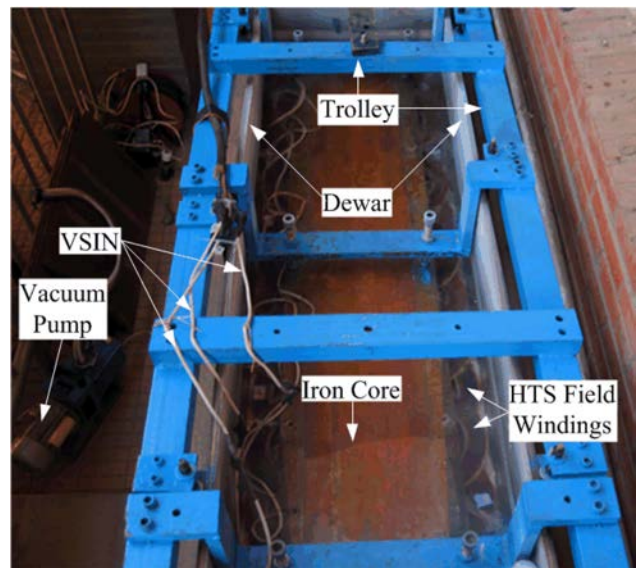

Fig. 3.   Practical prototype of the HTS LIM and the test bench.

liquid nitrogen. The secondary is a reaction plate and a back iron core. They are built using the aluminum sheet with a thickness of 3 mm and a steel sheet with a thickness of 8 mm, respectively.

To evaluate the performance of the HTS LIM, the practical prototype as well as the test bench were developed, as is shown in Fig. 3. The primary is hung in the bottom of the trolley, and the secondary is laid down in the middle of the two rails. While the windings are fed by the three-phase ac power supply, the thrust produced from the interaction between the primary magnetic flux and the eddy currents of the secondary will drive the trolley forward.

The main specifications and parameters of the prototype are listed in Table I.

In the prototype, the primary is hanging below the vehicle, which increases the complication of the machine construction

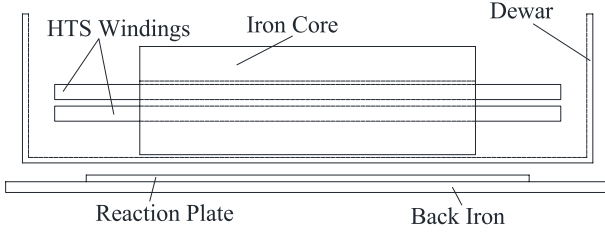| Items/units	Value
Core length/mm	1551.2
Core height/mm	80
Core width/mm	250
Slot depth/mm	42
Slot width/mm	47.2
Slot number	26
Number of poles	8
Windings connection	Y
Material of the HTS windings	Bi-2223/Ag

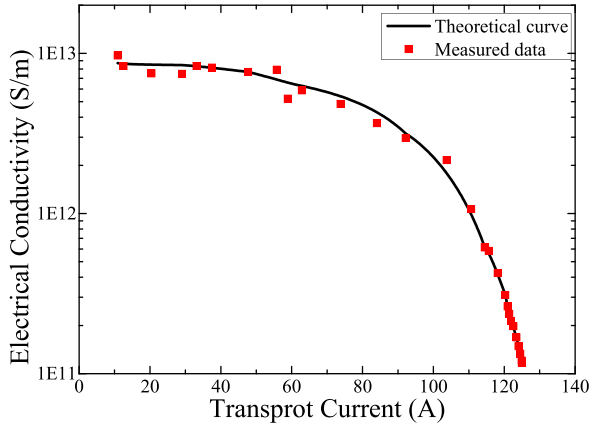Fig. 4.   General left overview of the developed prototype.

Fig. 5.   Equivalent electrical conductivity of the HTS tape.

with totally enclosed Dewar. Thus, a Dewar with an open top as shown in Fig. 4 was designed. The machine is cooled by the natural evaporation of the liquid nitrogen.

B. Equivalent Electrical Conductivity of the HTS Tape

The E–J characteristic of the HTS tape is given in (1) [18]

$$E = E_c \left(\frac{J_{sc}}{J_c \left(|B|, T \right)} \right)^n. \tag{1}$$

Usually, the operating temperature is constant. Thus, the influence of the temperature on the transport current density could be ignored. Derived from (1), the equivalent electrical conductivity could be calculated by

$$\sigma_{sc} = \frac{J_{sc}}{E} = \frac{J_c \left(|B| \right)}{E_c} \left(\frac{J_c \left(|B| \right)}{J_{sc}} \right)^{n-1} \tag{2}$$

where E is the terminal voltage of the HTS windings, E_c is the critical electric field, $E_c = 1.0 \times 10^{-4}$ V/m, J_c is the critical current density, $J_c = 1.04 \times 10^8$ A/m^2, J_{sc} is the transport current density, and n is the coefficient.
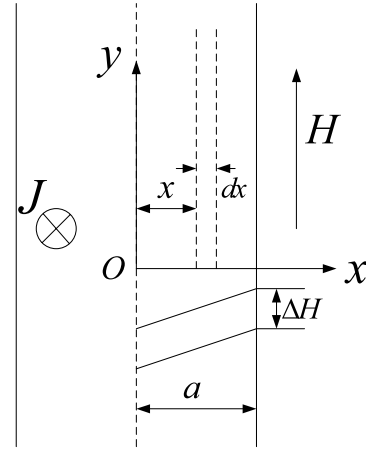

Fig. 6.   General configuration of the HTS tape.

The experiment was carried out on a short sample of the HTS tape. While the ac is applied to the sample, the terminal voltage between the two terminals could be measured. The electrical conductivity of the HTS tape could be obtained from the relation of the terminal voltage with the transport alternating current and the sectional area. The comparison of the calculated equivalent electrical conductivity and the measured data are shown in Fig. 5. It shows that the theoretical curve agrees with the measured data.

C. Equivalent Magnetic Permeability of the HTS Tape

Usually, the external magnetic flux density is larger than the minimal critical magnetic flux density of the superconductor operating at the critical state. The magnetic flux is pinned by the impurities the superconductor is doped with. The magnetic permeability is proposed to describe the magnetic flux pinning phenomenon, what can make the electromagnetic calculations easier [23], [24]. In this paper, the section dimension of the HTS tape is 4.3 mm × 0.24 mm. The aspect ratio is larger than 10. The HTS tape could be considered as an infinite plane with a finite thickness, as shown in Fig. 6. The following assumptions are proposed to simplify the calculation.

1) The magnetic field intensity in the HTS tape denoted as H_i, is based on the critical state Bean model, with the superconducting current density given by (3)

$$J_c \left(|H_i| \right) = J_{c0} \tag{3}$$

where $J_c \left(|H_i| \right)$ is the penetrated superconducting current density and J_{c0} is the critical current density.

2) The external magnetic field intensity is parallel to the tapes.

3) The magnetic flux penetrates gradually inward the tapes as the external magnetic field intensity increases.

The internal magnetic field intensity is obtained from the Maxwell's equation

$$H_i = H + J_c \left(x - a \right), \quad x \geq 0. \tag{4}$$

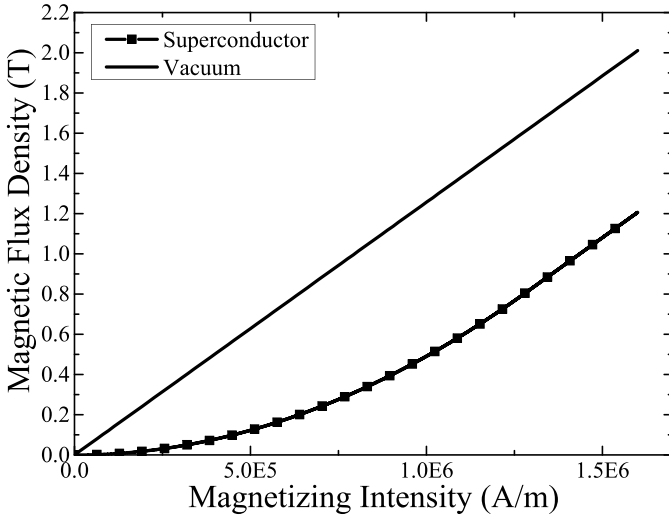$$H_i|_{x=0} = H - J_c a = 0. \tag{5}$$

Fig. 7. Relationship of the magnetic flux density with the magnetizing intensity.

While the HTS superconductors are fully penetrated by the external flux density, using the boundary conditions given by (5), the magnetic field intensity H_p

$$H_p = J_c a. \tag{6}$$

The average magnetizing intensity of the HTS tape could be calculated from (7) as

$$-M(H) = H - \frac{1}{V} \int_V H_i dV = H - \frac{1}{a} \int_0^a H_i(x) dx. \tag{7}$$

The relation of the magnetic flux density with the magnetization and magnetic field intensity are given by (8)

$$B(H) = \mu_0(M + H). \tag{8}$$

Substituting (8)–(11) into (9), the final result is

$$B(H) = \begin{cases} \frac{\mu_0 H^2}{4H_p}, & H \le H_p \\ \frac{\mu_0 H_p}{4}, & H \ge H_p \end{cases}. \tag{9}$$

Compared with the magnetic permeability of the vacuum, the magnetic permeability of the HTS tape is shown in Fig. 7. It shows that the relative magnetic permeability of the HTS is less than that of the vacuum.

D. Mathematical Model for the HTS LIM

Due to the limited primary, the winding turns mounted in the middle poles differ with that in the end poles. For double-layer windings, the turns in the end poles are half of that in the middle poles, and this effect is called the half filled slots effect; while for single-layer windings there will be two empty slots in the first pole and the last pole, e.g. in Fig. 2, the No. 2 and No. 25 slots are empty. This effect is similarly called the empty slot effect. The parameters of the LIM change with the speed, and they are also affected by the end effects and the half-filled slots. The calculation theories and methods proposed for RIM are not accurate for flux density distributions and performance analysis of the HTS LIM [11]. However, the FEM

could account for the above phenomenon. It is introduced to solve the magnetic flux distribution and the performances of the motor [3], [4], and [15]. The following assumptions make the mathematical model simpler [25], [26].

1) The displacement current and the harmonics caused by the source current are ignored, and the source current and eddy current only have the components along the z-axis.
2) The temperature sensibility effect of the resistivity and the permeability is ignored.
3) The leakage magnetic flux of the back side of the iron core is ignored.
4) The current density in the superconductors is evenly distributed.

The solving region of 2-D transient electromagnetic field is shown in Fig. 8. The Ω is the solving region, S_1 is the boundary of the magnetic field, where the magnetic field is regarded zero, S_2 is the backside of the iron core, S_3 is the interface between the reaction plate and the back iron.

Based on the Maxwell's equations and the Ohm's law in moving medium, the 2-D mathematical model and its boundary conditions are given below using the magnetic vector potential A[3].

In the non-eddy-current region

$$\begin{cases} \Omega: \frac{\partial}{\partial x}\left(\frac{1}{\mu}\frac{\partial A_z}{\partial x}\right) + \frac{\partial}{\partial y}\left(\frac{1}{\mu}\frac{\partial A_z}{\partial y}\right) = -J_s + \sigma\frac{\partial A_z}{\partial t} \\ S_1, S_2: A_z = 0 \end{cases}. \tag{10}$$

In the eddy-current region

$$\begin{cases} \Omega: \begin{cases} \frac{\partial}{\partial x}\left(\frac{1}{\mu}\frac{\partial A_z}{\partial x}\right) + \frac{\partial}{\partial y}\left(\frac{1}{\mu}\frac{\partial A_z}{\partial y}\right) = -J_e \\ J_e = \sigma\left[-\frac{\partial A_z}{\partial t} + (1-s)v_s \times (\nabla \times A_z)\right] \\ v_s = 2f\tau \end{cases} \\ S_1: A_z = 0 \\ S_3: \frac{1}{\mu_1}\frac{\partial A_z}{\partial n} - \frac{1}{\mu_2}\frac{\partial A_z}{\partial n} = K \end{cases} \tag{11}$$

where A_z is the magnetic vector potential, μ is the magnetic permeability, J_s is the source current density, J_e is the eddy-current density, σ is the electrical conductivity, v_s is the synchronous speed, and s is the slip. f is the rated frequency, τ is the pole pitch, μ_1 and μ_2 are the relative permeability, and K is surface current density.

The mathematical model is discretized and solved using the Galerkin FEM. The solution flow diagram is shown in Fig. 9. In the iterative calculation, σ_{sc-new} is calculated by (2), ε is the convergence coefficient, here it is set to 0.01.

III. CALCULATED RESULTS AND ANALYSIS

A. Distributions of the Magnetic Flux Density

While the iterative calculation is done, the magnetic flux distributions are shown in Fig. 10. The pinning force produced by the pinning centers suppresses the external magnetic flux penetrating the superconductor. Thus, the magnetic flux density in the HTS windings is lower than that in other motor components. In addition, affected by the end-effect and the empty slots effect, the magnetic flux density in the end region is lower than that in the middle poles. Moreover, the magnetic flux density in the exit end is larger than that in the entrance
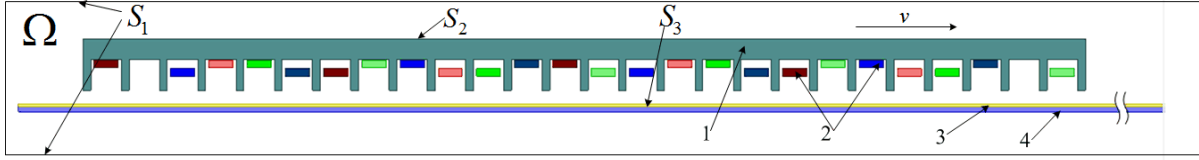
Fig. 8.   Solving region for the HTS LIM with a slotted iron core. 1: Slotted iron core. 2: HTS windings. 3: Reaction plate. 4: Back iron core.

end, which corresponds with the results as presented in [27]. The magnetic flux distribution of the HTS windings is shown in Fig. 10(b). It shows that the magnetic flux density in the lower part is larger than that in the upper part, which is caused by the leakage magnetic flux in the slot.

Fig. 11 shows the air-gap magnetic flux density and its harmonic analysis. The teeth-slot effect has a great influence on the air-gap magnetic flux density. For the motor designed with full pitch windings, the fifth harmonics is larger than other harmonics. To obtain a good performance, the measures should be taken to suppress the harmonics.

B. Steady-State Performance of the HTS LIM

The steady-state performance can be obtained from the FEM solution. The force in each element can be obtained, and the total force characteristics could be calculated by summation of all the elements. While the motor is operated in a steady state, the average force in one cycle could be calculated as follows [28], [29]:

$$F_{\text{thrust}} = \frac{1}{T_e} \int_t^{t+T_e} L_{ef} \cdot \sum_{i=1}^{n} B_{yi} \cdot J_{zi} S_i dt \qquad (12)$$

$$F_{\text{nomal}} = F_{y1} + F_{y2} \qquad (13)$$

$$F_{y1} = \frac{1}{T_e} \int_t^{t+T_e} L_{ef} \cdot \sum_{i=1}^{n} B_{xi} \cdot J_{zi} S_i dt \qquad (14)$$

$$F_{y2} = \frac{\partial W_m}{\partial g_e} = \frac{1}{T_e} \int_t^{t+T_e} \frac{\partial}{\partial g_e} \frac{L_{ef}}{2\mu_0} \sum_{i=1}^{n} B_{yi}^2 S_i dt \qquad (15)$$

where the F_{thrust} is the thrust of the motor, B_{xi} and B_{yi} are the x and y components of the magnetic flux density, respectively, J_{zi} is the eddy-current density, S_i is the area of the element i, T_e is a cycle time, F_{nomal} is the vertical force, F_{y1} is the repulsive force produced by eddy current and the source current, F_{y2} is the attractive force produced by primary magnetic field and the ferromagnetism in secondary, W_m is the energy of the magnetic field, g_e is the length of the air-gap, μ_0 is the permeability of the vacuum, and n is the total number of the meshed elements.

While the motor is operated with different slip, the force characteristics are shown in Fig. 12. The thrust decreases with the reduced slip, while the vertical force increases as the slip is reduced. In the entire slip, the vertical force is an attractive force. In the lower slip, the vertical force is very large, which would increase the resistance of the motor. Therefore, we should pay more attentions to the vertical force.

In the developed prototype, the ac loss of the HTS windings is almost zero. The loss of the motor is mainly determined by the eddy-current loss in the reaction plate and the back iron
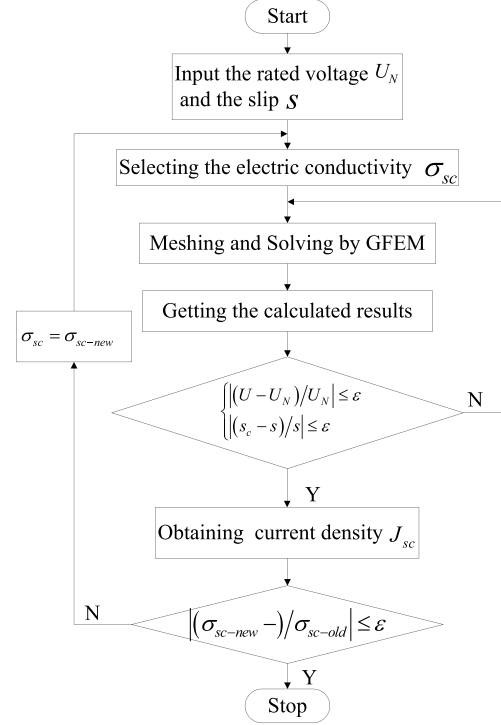

Fig. 9.   Solving flow diagram for the HTS LIM.

plate. The total eddy-current loss P_{eddy} are calculated by (11) in a cycle [26]

$$P_{\text{eddy}} = \frac{1}{T_e} \int_t^{t+T_e} \frac{L_{ef}}{\sigma} \sum_{i=1}^{n} J_{zi}^2 S_i dt \qquad (16)$$

where σ is the electrical conductivity and J_{zi} is the eddy-current density.

Obtained from the FEM solution, the eddy-current loss is shown in Fig. 13. When the motor is operated with the locked-primary state, the loss is ~6000 W, whereas the loss is rapidly reduced to 624 W when the motor is operated at a speed next to the synchronous speed, ~10% of that in locked-primary state.

The power factor $\cos(\varphi)$ and the efficiency η could be calculated from (17)

$$\begin{cases} \cos(\varphi) = \cos(\varphi_1 - \varphi_2) \\ \eta = (F_{\text{thrust}} \times (1-s)v_s)/(\sqrt{3}U_N I_P \cos(\varphi)) \end{cases} \qquad (17)$$

where φ_1 and φ_2 are the electrical angle of the terminal voltage and the phase current and I_P is the calculated phase current under the given slip s.

The calculated power factor and efficiency are shown in Fig. 14. The power factor decreases with the slip.
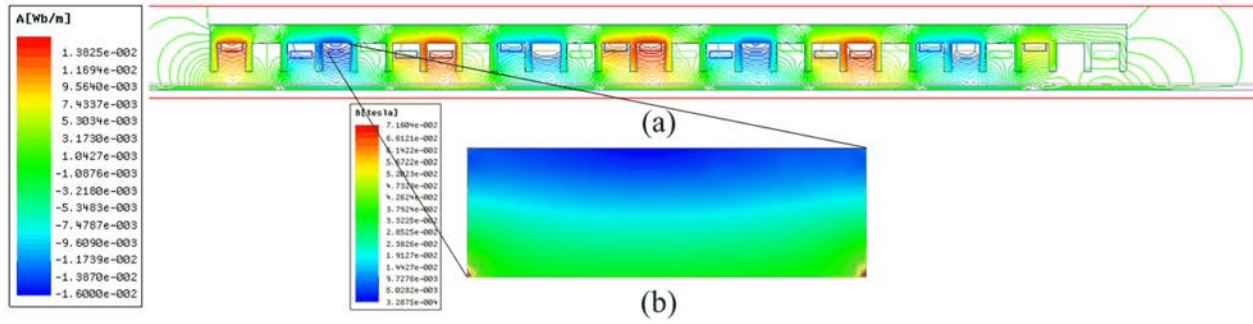
Fig. 10. Magnetic flux distribution of the HTS LIM. (a) Magnetic flux distribution of the entire motors. (b) Magnetic flux distribution of the HTS windings.
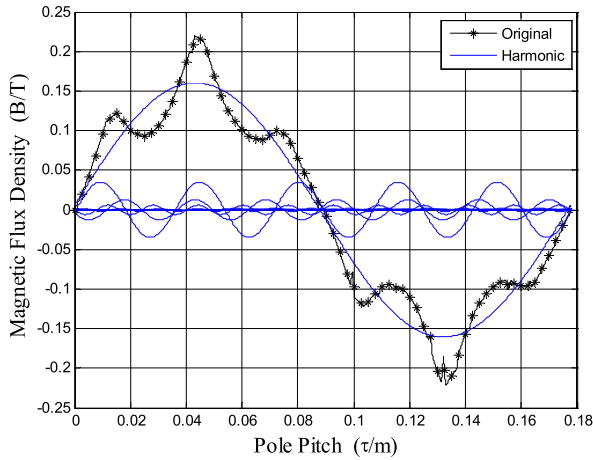

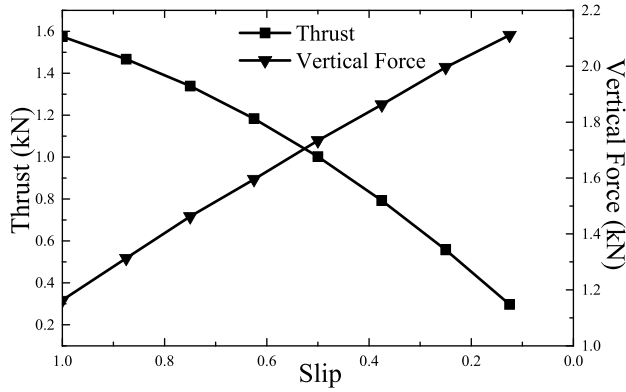Fig. 11. Air-gap magnetic flux density and the harmonic analysis.

Fig. 12. Relationships of the force characteristics with slip.

Fig. 13. Curve of the eddy-current loss with slip.
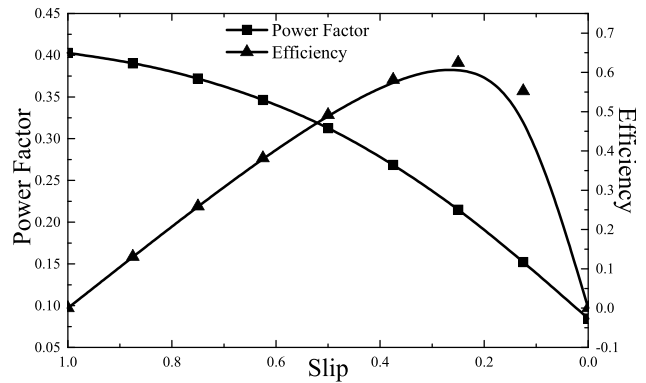
Fig. 14. Relationships of the power factor and the efficiency with slip.

The maximum efficiency is about 0.62 while the motor is operated with a slip of about 0.25.

C. Critical Current Evaluation of the HTS LIM

The critical current decreases with the external magnetic flux density increasing. While the motor is operated, the slot leakage flux changes with the slip, the critical current of the HTS tapes will also change with the slip. Therefore, it is important to evaluate the critical current of the motor with different state. It is different to measure the critical current while the motor is operated. Thus, the influence of the external magnetic flux on the critical current is evaluated indirectly.
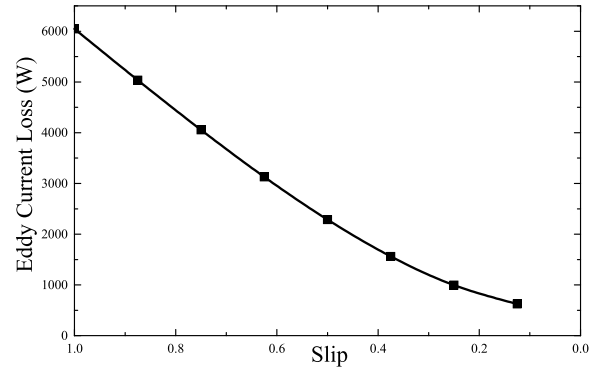
Initially, the relation of the critical current to the external magnetic flux density should be tested. The specifications of the practical HTS tapes have been listed in Table II. The relation of the critical current to the external flux density are shown in Fig. 15. The critical current decreases monotonically with the external magnetic flux density increasing. The decrease of the critical current with the perpendicular magnetic flux density is larger than that with the parallel magnetic flux density.

The maximum of the parallel components (parallel to wide side of HTS tapes) and the perpendicular components (perpendicular to the wide side of HTS tapes) of the magnetic flux

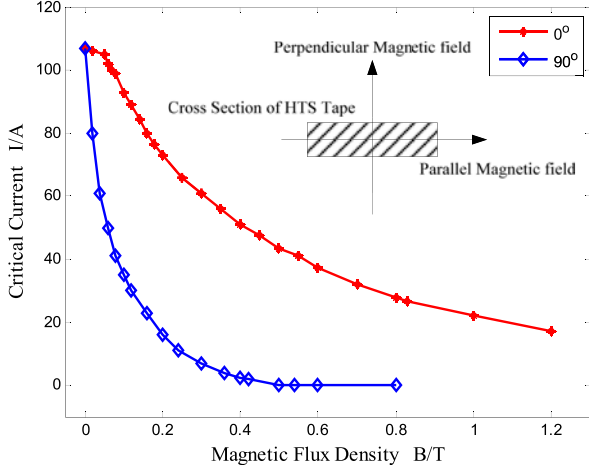| Items	Value
Sectional area(bare)	4.3mm×0.24 mm
Insulation resistance	1000 MΩ
Breakdown voltage	800V
Allowable bending radius	30mm
Critical current(77K,self-field)	107A

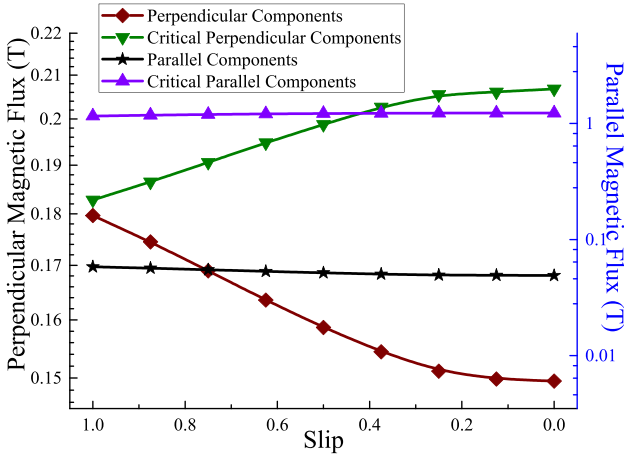Fig. 15.   Relationship of the critical current with the external flux density.

Fig. 16.   Curves of the flux density and the critical values with the slip.

Fig. 17.   Constructed testing bench for the HTS LIM.

density around the windings could be calculated by

$$\begin{cases} B_{//} = \max(B_{yi}) \\ B_{\perp} = \max(B_{xi}) \end{cases} \tag{18}$$

where $B_{//}$ and $B_{\perp}$ are the parallel components and perpendicular components of the magnetic flux density, respectively. B_{xi} and B_{yi} are the magnetic density of the element i in x- and y-axis, respectively.

The comparison between the critical components of the magnetic flux density obtained from the measured data and the maximum of the leakage flux density around the windings are shown in Fig. 16. The perpendicular component of the magnetic flux density increases with the slip decreasing.
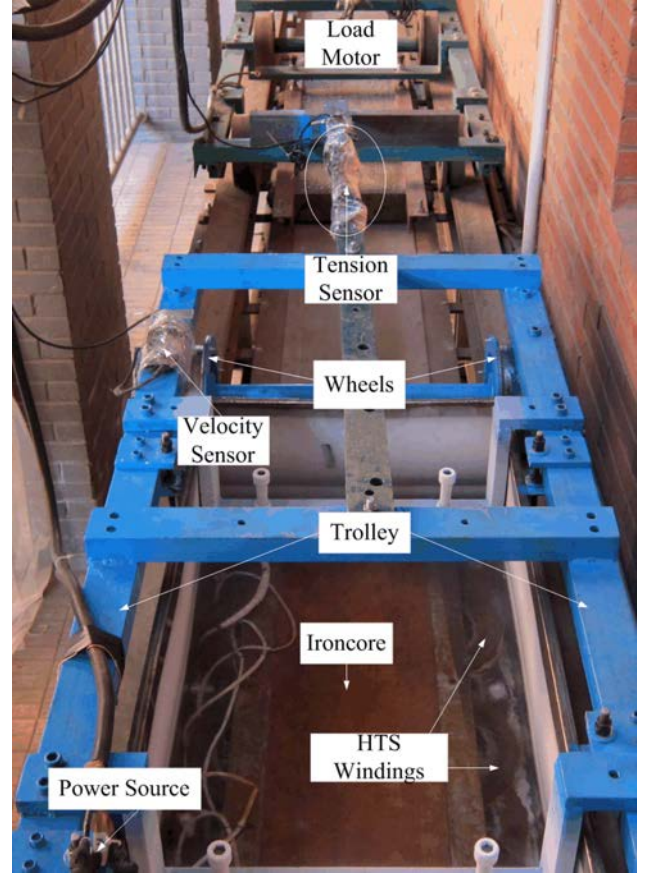
However, the parallel component almost has a few changes in the entire slip region. The magnetic flux density is less than the critical components of the magnetic flux density. The motor could be operated safely in the entire slip region, but the safety margin is too small in the high slip region. Therefore, in the actual applications this operation state should be avoided. The parallel component is far less than the critical parallel magnetic flux density. While the motor is designed, the influence of the parallel magnetic flux density on the critical current could be ignored.

IV. EXPERIMENT OF THE HTS LIM

To validate the accuracy of the simulation results, the experiment has been carried out on the constructed prototype. Fig. 17 shows the testing bench. In the experiment, the prototype is connected with a LIM, with copper wire windings. The copper LIM is used as the load motor for the HTS LIM. The tension sensor is installed between the two motors. The velocity sensor is installed on the wheels. While the motor is operated with a balanced three-phase ac supply, the motor will accelerate and finally move with a steady speed.

Limited by the test bench to a 20 m rail, the motor could not reach the rated speed while it is driven at the rated frequency of 10 Hz. To obtain the steady performances of the motor, we tested the motor at a frequency of 4 Hz. The measured data could also be used to verify the accuracy of the
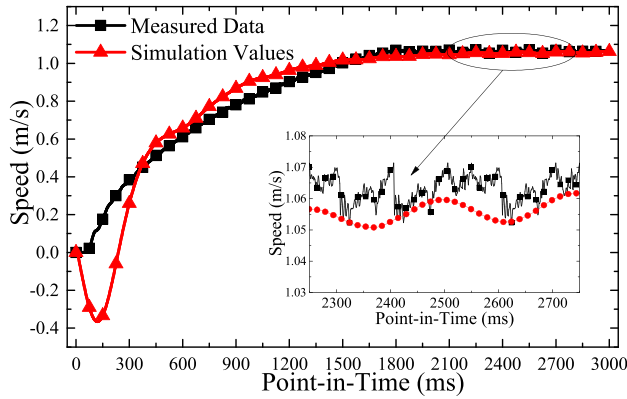
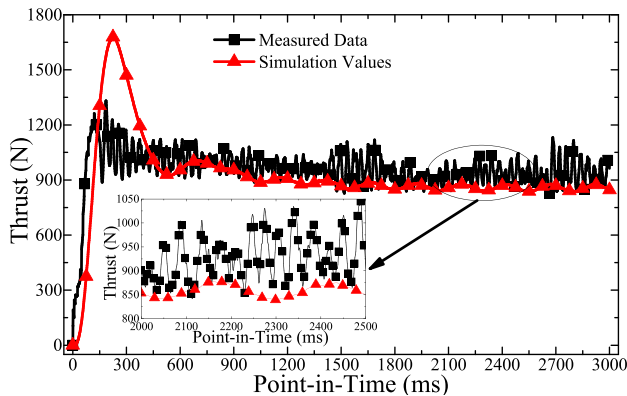Fig. 18. Speed curves of the measured data and the simulation values.

Fig. 19. Thrust curves of the measured data and the simulation values.

calculated method presented in this paper. The comparisons of the measured data with the simulated results are shown in Figs. 18 and 19. In the initial stage, the simulation results differ from the measured data; the reason could be explained as follows: 1) the load force in the experiment is the is static friction force existed between the wheels and the rails, whereas it is motive force in the simulation, which could drive the motor moving in the opposite direction and 2) influenced by the transverse end-effect, the leakage reactance of the actual motor is larger than that of the 2-D model.

While the motor is operated at a steady speed, the simulation results could correspond to the measured data. The differences of the speed and the thrust between the simulation results and the measured data are 0.7% and 7.7%, respectively. The speed meets the convergence conditions set in the FEM solution. The calculated thrust is slightly lower than the measured data. It is because that in the actual construction the secondary is developed wider than the primary, so the eddy current in the end zone also contributes to the thrust of the motor. Based on the analysis above, the established mathematical model is accurate for the calculation of the performance evaluation.

V. CONCLUSION

Based on the FEM, this paper sets out a new mathematical model for calculation and analysis of the HTS LIM, which considers the current characteristics and the magnetic flux

pinning phenomenon of the superconductor. The magnetic flux density distributions and the performance as thrust, vertical force, eddy-current loss, efficiency, and so on are calculated. Using comparisons between the simulation and the measured data, it follows that the established mathematical model can obtain accurate results for the motor.

In the future, the proposed mathematical model would be a crucial step for the electromagnetic optimization processes of the HTS LIM.

REFERENCES

[1] J. Fang, L. Sheng, D. Li, J. Zhao, S. Li, W. Qin, *et al.*, "Influence analysis of structural parameters and operating parameters on electromagnetic properties of HTS linear induction motor," in *Proc. 24th Int. Symp. Supercond.*, vol. 27. Oct. 2012, pp. 408–411.

[2] G. Jinlin, F. Gillon, and P. Brochet, "Magnetic and thermal 3D finite element model of a linear induction motor," in *Proc. IEEE VPPC*, Sep. 2010, pp. 1–6.

[3] H. Junfei, D. Yumei, L. Yaohua, J. Nengqiang, Z. Tiejun, and X. Wei, "Study and optimized design of stator core structure in single-sided linear induction motor," in *Proc. ICEMS*, Oct. 2008, pp. 3464–3469.

[4] B.-H. Lee, K.-S. Kim, J.-P. Hong, and J.-H. Lee, "Optimum shape design of single-sided linear induction motors using response surface methodology and finite-element method," *IEEE Trans. Magn.*, vol. 47, no. 10, pp. 3657–3660, Oct. 2011.

[5] A. Shiri and A. Shoulaie, "Design optimization and analysis of single-sided linear induction motor, considering all phenomena," *IEEE Trans. Energy Convers.*, vol. 27, no. 2, pp. 516–525, Jun. 2012.

[6] H. Hamzehbahmani, "Modeling and simulating of single side short secondary linear induction motor for high speed studies," *Eur. Trans. Electr. Power*, vol. 22, pp. 747–757, Sep. 2012.

[7] A. Zare Bazghaleh, M. R. Naghashan, and M. R. Meshkatoddini, "Optimum design of single-sided linear induction motors for improved motor performance," *IEEE Trans. Magn.*, vol. 46, no. 11, pp. 3939–3947, Nov. 2010.

[8] M. Mirsalim, A. Doroudi, and J. S. Moghani, "Obtaining the operating characteristics of linear induction motors: A new approach," *IEEE Trans. Magn.*, vol. 38, no. 2, pp. 1365–1370, Mar. 2002.

[9] X. Wei, Z. Jian Guo, Z. Yongchang, L. Yaohua, W. Yi, and G. Youguang, "An improved equivalent circuit model of a single-sided linear induction motor," *IEEE Trans. Veh. Technol.*, vol. 59, no. 5, pp. 2277–2289, Jun. 2010.

[10] X. Long, *Theory and Magnetic Design Method of Linear Induction Motor*. Beijing, China: Science Press, 2006.

[11] W. Xu, Y. H. Li, G. S. Sun, J. Q. Ren, L. C. Tan, K. Wang, *et al.*, "Performance study on high power linear induction motor in transportation," in *Proc. ICEMS*, vols. 1–4. 2007, pp. 103–105.

[12] A. H. Isfahani, B. M. Ebrahimi, and H. Lesani, "Design optimization of a low-speed single-sided linear induction motor for improved efficiency and power factor," *IEEE Trans. Magn.*, vol. 44, no. 2, pp. 266–272, Feb. 2008.

[13] M. Chen, L. Donzel, M. Lakner, and W. Paul, "High temperature superconductors for power applications," *J. Eur. Ceram. Soc.*, vol. 24, no. 6, pp. 1815–1822, 2004.

[14] S. Baik and Y. Kwon, "Electrical design of a 17 MW class HTS motor for ship propulsion," *J. Supercond. Novel Magn.*, vol. 26, pp. 1283–1287, 2013.

[15] S. K. Baik, Y. K. Kwon, H. M. Kim, S. H. Kim, J. D. Lee, Y. C. Kim, *et al.*, "Electrical parameter evaluation of a 1MW HTS motor via analysis and experiments," *Cryogenics*, vol. 49, no. 6, pp. 271–276, 2009.

[16] Y. K. Kwon, M. H. Sohn, S. K. Baik, E. Y. Lee, J. D. Lee, J. M. Kim, et al., "Development of HTS motor for industrial applications at KERI & DOOSAN," in Proc. IEEE Power Eng. Soc. General Meeting, Jan. 2006, pp. 1–8.

[17] M. H. Sohn, S. K. Baik, Y. S. Jo, E. Y. Lee, W. S. Kwon, Y. K. Kwon, et al., "Performance of high temperature superconducting field coils for a 100 HP motor," IEEE Trans. Appl. Supercond., vol. 14, no. 2, pp. 912–915, Jun. 2004.

[18] K. Yoshida and H. Matsumoto, "Propulsion and guidance simulation of HTS bulk linear synchronous motor taking into account E-J characteristic," Phys. C, Supercond., vols. 392–396, no. 1, pp. 690–695, 2003.

[19] J. Jian Xun, Z. Lu Hai, G. You Guang, Z. Jian Guo, C. Grantham, C. C. Sorrell, et al., "High-temperature superconducting linear synchronous motors integrated with HTS magnetic levitation components," IEEE Trans. Appl. Supercond., vol. 22, no. 5, pp. 5202617–5202620, Oct. 2012.

[20] J. Zhao, T. Q. Zheng, W. Zhang, J. Fang, and Y. M. Liu, "Influence analysis of structural parameters on electromagnetic properties of HTS linear induction motor," Phys. C, Supercond., vol. 471, no. 21, pp. 1474–1478, 2011.

[21] T. Famakinwa, Q. M. Chen, and S. Yamaguchi, "3D finite element analysis of eddy current loss of HTS tapes—External field analysis," Phys. C, vol. 459, pp. 18–23, Aug. 2007.

[22] P. J. Masson, P. Tixador, J. C. Ordonez, A. M. Morega, and C. A. Luongo, "Electro-thermal model for HTS motor design," IEEE Trans. Appl. Supercond., vol. 17, no. 2, pp. 1529–1532, Jun. 2007.

[23] D. X. Chen and R. B. Goldfarb, "Kim model for magnetization of type-II superconductors," J. Appl. Phys., vol. 66, no. 6, pp. 2489–2500, 1989.

[24] T. Torng and Q. Y. Chen, "Magnetic forces for type II superconductors in a levitation field," J. Appl. Phys., vol. 73, no. 3, pp. 1198–1200, 1993.

[25] A. H. Selcuk and H. Kurum, "Investigation of end effects in linear induction motors by using the finite-element method," IEEE Trans. Magn., vol. 44, no. 7, pp. 1791–1795, Jul. 2008.

[26] L. Weili, Q. Hongbo, Y. Ran, Z. Xiaochen, and L. Liyi, "Three-dimensional electromagnetic field calculation and analysis of axial-radial flux-type high-temperature superconducting synchronous motor," IEEE Trans. Appl. Supercond., vol. 23, no. 1, pp. 1–7, Feb. 2013.

[27] T. Yang, L. B. Zhou, and L. R. Li, "Influence of design parameters on end effect in long primary double-sided linear induction motor," IEEE Trans. Plasma Sci., vol. 39, no. 1, pp. 192–197, Jan. 2011.

[28] T. Yamada and K. Fujisaki, "Basic characteristic of electromagnetic force in induction heating application of linear induction motor," IEEE Trans. Magn., vol. 44, no. 11, pp. 4070–4073, Nov. 2008.

[29] T. Nakamura, H. Miyake, Y. Ogama, G. Morita, I. Muta, and T. Hoshino, "Fabrication and characteristics of HTS induction motor by the use of Bi-2223/Ag squirrel-cage rotor," IEEE Trans. Appl. Supercond., vol. 16, no. 2, pp. 1469–1472, Jun. 2006.

Dong Li was born in Nanyang, China, in 1987. He received the bachelor's degree from Zhengzhou Institute of Aeronautical Industry Management, Zhengzhou, China, in 2010. He is currently pursuing the Ph.D. degree in electrical engineering from the School of Electrical Engineering, Beijing Jiaotong University, Beijing.

His current research interests include the electromagnetic, fluid, and thermal analysis on the superconducting electric machines, especially on the high temperature superconducting linear induction motor used for subway system.

Weili Li received the master's degree from the Harbin Institute of Electrical Technology, Harbin, China, and the Ph.D. degree from Russia Electric Power Research Institute, St. Petersburg, Russia, in 1993 and 1997, respectively.

He is currently a Professor with the College of Electrical Engineering, Beijing Jiaotong University, Beijing. He has authored and co-authored more than 200 published refereed technical papers and he also holds 32 patents. His current research interests include synthesis physical field analyses on large electrical machines, renewable energy systems, and special electrical machine and associate control.

Jin Fang received the Ph.D. degree from Plasma Physics Institute, Chinese Academy of Science, Beijing, China, in 2002.

He is currently a Professor with the School of Electrical Engineering, Beijing Jiaotong University, Beijing. His current research interests include the design of superconducting wire, cable and superconducting magnets, superconducting magnetic levitation devices, and superconducting motors as well as in the research of stability and AC loss of superconducting material.

Xiaochen Zhang (S'09–M'12) received the master's degree from the Harbin University of Science and Technology, Harbin, China, and Ph.D. degree from the Harbin Institute of Electrical Technology, Harbin, in 2006 and 2012, respectively.

He is currently with the School of Electrical Engineering, Beijing Jiaotong University, Beijing. His current research interests include the design, theory analysis, and the synthesis physical field analysis on PM electric machine and high-speed machines.

Junci Cao (M'09) received the master's degree from the Harbin University of Science and Technology, Harbin, China, and the Ph.D. degree from the Harbin Institute of Electrical Technology, Harbin, in 2004 and 2008, respectively.

He is currently with the College of Electrical Engineering, Beijing Jiaotong University, Beijing. His current research interests include the design, theory analysis, and the synthesis physical field analysis on special electrical machine.